JOURNAL OF GEOPHYSICAL RESEARCH, VOL. 105, NO. D15, PAGES 19,973–19,990, AUGUST 16, 2000

Numerical simulations of the July 10 Stratospheric-Tropospheric Experiment: Radiation, Aerosols, and Ozone/Deep Convection Experiment convective system: Kinematics and transport

William C. Skamarock,[1] Jordan G. Powers,[1] Mary Barth,[1] James E. Dye,[1] Thomas Matejka,[2] Diana Bartels,[2] Karsten Baumann,[1,3] Jeffrey Stith,[4,5] David D. Parrish,[6] and Gerhard Hubler[6]

Abstract. The observed July 10, 1996, Stratospheric-Tropospheric Experiment: Radiation, Aerosols, and Ozone (STERAO) convective system is broadly reproduced in a nonhydrostatic cloud model simulation using an idealized horizontally homogeneous sounding and no terrain. System evolution from a multicellular line to a supercell, along with line orientation, anvil structure, horizontal wind fields, depth of convection, and derived radar reflectivity, compares well with observations. Simulated passive tracer transport of CO and ozone generally agrees with aircraft measurements and shows a small amount of entrainment of environmental air in the updrafts, and a small amount of dilution occurring with transport downwind in the anvil; the entrainment and dilution are less pronounced in the supercell stage. The horizontally integrated vertical flux divergence for CO in the simulation shows a net gain at almost all levels above 8 km mean sea level (msl). The rate of increase of CO mass above 8 km varies significantly in time, with a peak at early times, followed by a decline and minimum as the system transitions to a supercell and a steady increase as the supercell matures. Trajectory analyses show that updrafts in the simulation are ingesting air from a layer spanning from 2 km to 3.5 km msl (from 0.5 to 2 km above the surface). The residence times for parcels in the updraft varies from just under 10 min to more than 20 min, with most parcels taking approximately 10 min to ascend to the anvil.

1. Introduction

The Stratospheric-Tropospheric Experiment: Radiation, Aerosols, and Ozone (STERAO)/Deep Convection project, whose observational component was conducted in June and July 1996 in northeastern Colorado, has as a major objective to investigate thunderstorms' role in the distribution of chemical species in the troposphere. Of particular concern is the evolution of water vapor and odd nitrogen species in the troposphere and lower stratosphere [*Dye et al.*, 2000]. While one of the specific concerns is the examination of NO_x (= NO + NO_2) production by lightning and NO_x transport by convective and mesoscale circulations, a more general concern is quantifying the net convective transport of boundary layer species into the troposphere and lower stratosphere, particularly as a function of the structure of the evolving convective systems. We wish to improve our understanding of chemical transport on both the convective scale and the mesoscale, for application in cloud chemistry and longer-time scale studies, and potentially for use in convective transport parameterizations in larger-scale models. To these ends, we employ a three-dimensional (3-D) cloud model to simulate the July 10, 1996, STERAO convective event and analyze tracer transport within the simulated system.

The character of tracer transport in midlatitude and tropical convective systems, as revealed in observational and modeling studies, has been found to vary significantly among different convective events and often varies temporally as convective systems evolve. The transport of boundary layer air into anvils, entrainment and detrainment in updrafts, and exchange of air across the tropopause have received the most attention in the studies. In midlatitude continental convective storms, *Hauf et al.* [1995] found largely undiluted boundary layer air transported to the anvil in 3-D simulations of supercell storms observed over central Europe. Alternatively, *Wang and Chang* [1993] and *Wang and Crutzen* [1995] found that considerable dilution of boundary layer air occurs as it is transported through the updrafts into the anvil in 3-D and 2-D simulations of midcontinental (United States) convective storms. In the 3-D modeling study by *Wang and Chang* [1993], significant change in both the transport characteristics of the storm and the boundary layer

[1] National Center for Atmospheric Research, Boulder, Colorado.
[2] NOAA Severe Storms Laboratory, Boulder, Colorado.
[3] Now at the School of Earth and Atmospheric Science, Georgia Institute of Technology, Atlanta.
[4] Department of Atmospheric Sciences, University of North Dakota, Grand Parks.
[5] Now at the National Center for Atmospheric Research, Boulder, Colorado.
[6] NOAA Aeronomy Laboratory, Boulder, Colorado.

Paper number 2000JD900179
0148-0227/00/2000JD900179$09.00

source region for updrafts occurs in the simulations. In modeling studies of oceanic and continental tropical convection, *Wang et al.* [1995] and *Scala et al.* [1990] found significant dilution of boundary layer air as it is transported in convective updrafts and in the anvil; Scala et al. found that greater than 50% of the air transported into the anvil originates from above the 6 km level in their 2-D simulations of the May 6, 1987, Amazon Boundary Layer Experiment (ABLE) 2B storm. *Wang et al.* [1995] found that significant amounts of stratospheric air can be brought into the tropospheric cloud region, particularly in the upper anvil. This wide range of results in part reflects the different character of the convective storms and the different emphases of the studies.

Most studies of tracer transport in convective systems that are based on cloud-resolving simulations have assumed two-dimensionality, that is, the convective lines are assumed not to vary in the along-line direction, and two-dimensional simulations are employed [e.g., *Wang et al.*, 1995; *Pickering et al.*, 1992a; *Scala et al.*, 1990]. The 2-D assumption, however, is appropriate only for environments with little hodograph curvature, for long convective lines, or for lines with short lifetimes [*Skamarock et al.*, 1994] that is, valid only for a small subset of observed convective systems. Observations show that the July 10 STERAO system was not two-dimensional or even quasi-two-dimensional during any stage of its evolution. Through its middle stages the system was multicellular, consisting of two to four cells oriented NW–SE [*Dye et al.*, 2000]. The orientation of the line of cells was more parallel to the low-level shear than perpendicular to it, and the anvil outflow was predominantly parallel to the line (i.e., it streamed toward the southeast). The orientations of both the line and the anvil, therefore, were contrary to a 2-D configuration. The system's final stage featured a single, large, convective cell propagating south-southeastward. Although not as long-lived as most supercells, the single cell in the final stage was supercellular in character (possessing low-level and midlevel rotation, verified by ground and aircraft observers and Doppler analyses, and possessing a single, long-lived updraft) and contained highly 3-D dynamics and airflow.

Using a fully 3-D model and beginning with a horizontally homogeneous sounding derived from observations, we have produced a simulated convective system that captures the observed evolution of the July 10 storms. In particular, the transition from a multicellular line to a single supercell is reproduced. The characteristics of the transport by convective updrafts are in some respects similar to those seen in results from previous studies. For example, there is some entrainment in the active updrafts, more pronounced in the multicellular regime [e.g., *Scala et al.*, 1990] than in the the supercellular regime [e.g., *Hauf et al.*, 1995] Furthermore, in accord with *Wang and Chang* [1993] we find that the character of the transport varies significantly in time as the system evolves. We document the transport from both a convective-scale viewpoint, primarily using trajectory analyses, and from a larger-scale viewpoint, by examining the horizontally integrated vertical flux divergence, a quantity parameterized in larger-scale models.

2. Meteorological Overview

The July 10 convective system developed near the southern Wyoming–Nebraska border along a topographic feature known as the Cheyenne Ridge. Building during late afternoon (local time) on July 10, the main cells propagated south-southeastward into northeastern Colorado before dissipating in the evening.

At 0000 UTC, July 11 (i.e., during the event, 1800 MDT, July 10, local time) synoptic conditions were characterized by a broad ridge over the convective area. At upper levels a shortwave trough, propagating eastward, extended in a southwest-northeast orientation from western Kansas to eastern Nebraska, as indicated by the dashed line in the 300 mbar analysis in Figure 1. While this wave had moved across northeastern Colorado from 1200 to 0000 UTC, July 10–11, its passage over the area was too early to serve as a forcing mechanism for the convection under study. During this period the shortwave's progression was attended by a shift in the 300–500 mbar winds over the convective area from westerly to northwesterly and a weakening of the flow through this depth. Anvil-level (e.g., 200 mbar) flow remained westerly through 0000 UTC, however.

The main surface feature in the region was a stationary front extending southward from the Wyoming-Nebraska border into eastern Colorado. As seen in Figure 1, at 2100 UTC, July 10, the frontal boundary separated cool, relatively moist air in Nebraska and eastern Colorado from warmer, drier air in Wyoming and central Colorado. At 2100 UTC on July 10 dew points on the cool side were 13°–16°C, while those to the west (warm side) were 3°–10°C. The surface flow was southerly-southeasterly on the cool side, with stations in eastern Colorado and western Kansas and Nebraska reporting cloudy conditions (satellite imagery presented below). The latter areas also had fog and light rain. A surface mesonet, active in northeastern Colorado during the STERAO campaign, revealed a north-south gradient in surface moisture, with decidedly higher dew points (15°–16°C) north of about 40°N latitude and lower dew points ($\leq$ 10°C) south of about 40°N.

The National Weather Service sounding from 0000 UTC on July 11 (not shown) reveals a dry, deep, well-developed planetary boundary layer (PBL) on the warm side of the front in Denver, (DEN; located in Figure 1a), with a surface temperature of 30°C and water vapor mixing ratios of approximately 5.5 g kg^{-1} in the PBL; no frontal inversion appears. In contrast, the Scottsbluff sounding (BFF; located in Figure 1a) in the frontal zone at 0000 UTC showed a surface temperature of 22°C and PBL mixing ratios of 9–12 g kg^{-1}. The sounding penetrated the frontal surface at 800–700 mbar, which presented a deep, strong cap to surface-based convection.

Satellite imagery from the afternoon (local time) of July 10 through the early evening reveals the evolution of the convection. At 2202 UTC (Figure 2a), low cloud prevailed over easternmost Colorado, southwestern Nebraska, and western Kansas. In contrast, a cloud-free swath lay to the west and extended southward from the Wyoming–Nebraska border.

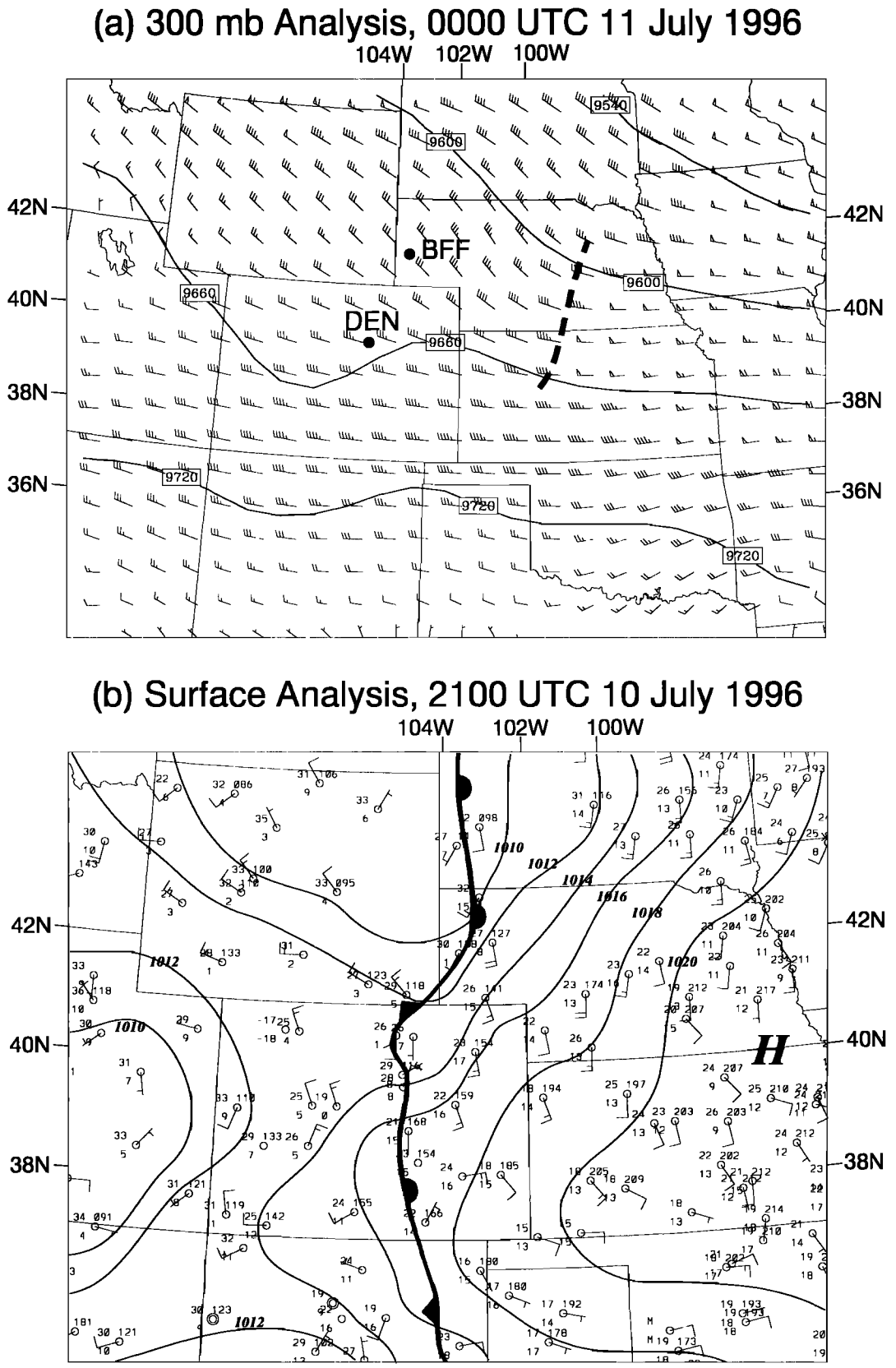

Figure 1. (a) The 300 mbar analysis for 0000 UTC on July 11, 1996, and (b) surface analysis for 2100 UTC on July 10, 1996. In the 300 mbar analysis, solid contours are heights (contour interval is 60 m). In the surface analysis, the solid contours are surface pressure (contour interval is 2 mbar), and the surface observations are plotted using the standard convention (for winds, a full barb equals 10 knots or 5.1 $m\,s^{-1}$). Temperatures and dew points are in degrees Celcius.

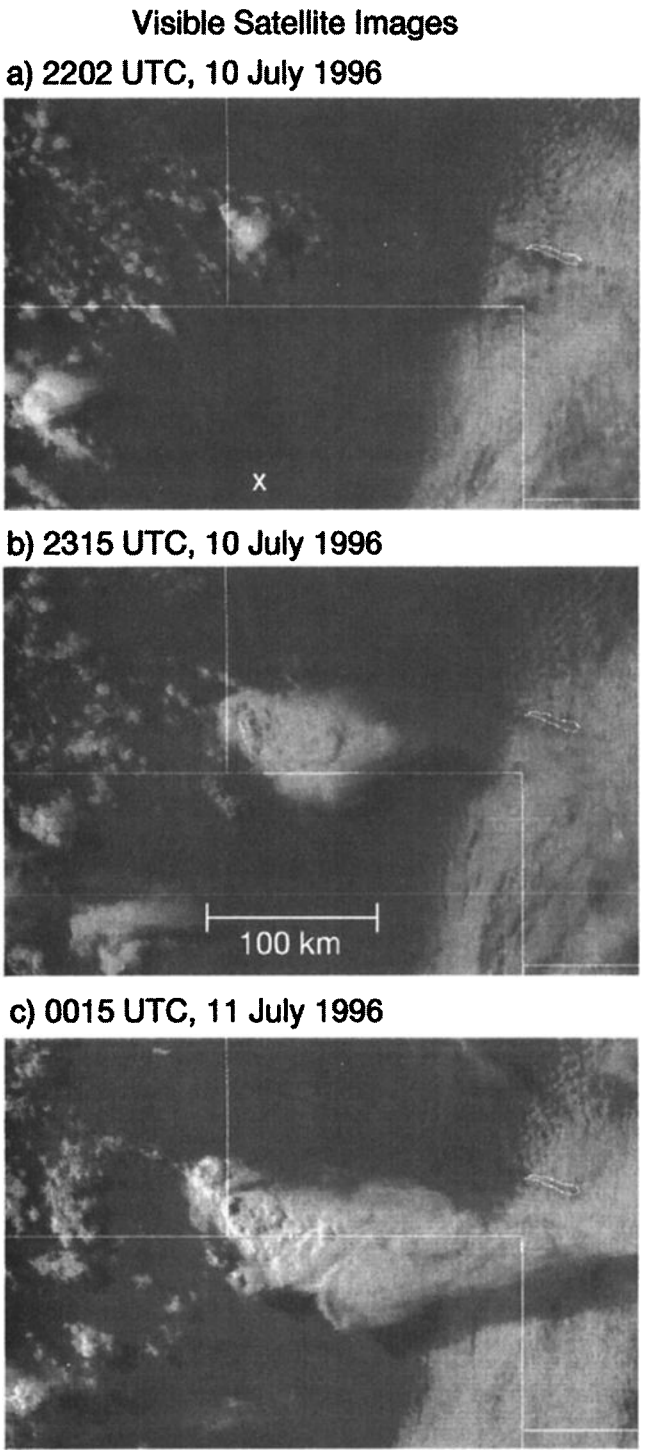

Figure 2. Visible satellite images for the July 10 STERAO storm. The map background shows the intersection of the Colorado, Nebraska, and Wyoming borders slightly to the left of center, with a very small portion of Kansas visible in the lower right corner. The CLASS sounding was taken at the location marked by a cross in Figure 2a .

By this hour, small cumuli have developed on the Cheyenne Ridge, and the clouds' delineation of, and conformation to, the topography suggests that the convection is being forced by elevated heating and upslope low-level flow (southerly flow encountering the W-E oriented Cheyenne Ridge). Apparent on the eastern edge of the ridge at the Wyoming-Nebraska border is the anvil from the incipient convective system.

At 2315 UTC (Figure 2b) the multicellular character of the convection is apparent and the anvil has expanded to the east. By 0015 UTC on July 11 (Figure 2c), the strongest updrafts were located just north and east of the Wyoming–Colorado–Nebraska intersection. The anvil from this convection had expanded significantly in the preceding 2 hours and continued to move eastward after this time. The imagery in Figure 2c highlights the relative height of the anvil, which is casting a shadow over the low-level cloud over eastern Colorado and southwestern Nebraska. The area just south of the Cheyenne Ridge, in northeastern Colorado, has remained essentially clear throughout the episode, further evidence that the forcing was topographic.

3. Model Initialization

The fully compressible 3-D nonhydrostatic cloud model used in this study, the Collaborative Model for Multiscale Atmospheric Simulation (COMMAS), is derived from the model described by *Wicker and Wilhelmson* [1995]. It has been modified to use the second-order Runge-Kutta time integration algorithm described by *Wicker and Skamarock* [1998] and the ice microphysics from the Goddard Cumulus Ensemble Model described by *Tao and Simpson* [1993]. The scalar quantities in the model, including the mixing ratios of the water species (vapor, cloud water, rain, ice, snow, and hail, with hail density $\rho_h = 0.9\,\mathrm{g\ cm^{-3}}$ and hail number concentration $N_o = 4 \times 10^4\,\mathrm{m^{-4}}$) and the passive chemical species (CO and O_3), are advected using a modified Van Leer type scheme that is monotonic [see *Wicker and Wilhelmson*, 1995].

The model environment is initialized with a horizontally homogeneous thermodynamic sounding, and a flat lower boundary (i.e., no topography) is employed. Neither the effects of radiation nor surface moisture and heat fluxes are included. Our rationale for these simplifications is that we are modeling the convective and mesoscale environment and not the mesoscale or synoptic-scale forcing that produced the environment. Outside of establishing the convective environment, the large-scale synoptic evolution and effects of terrain are considered to have only a small impact on the convective evolution, although the topography certainly played a role by producing an isolated, elevated heating source and possibly a region of orographically induced low-level lifting (that would explain the occasional generation of new cells at the northwest edge of the line). The fidelity of the simulations to the observations, demonstrated below, strongly suggests that topographic effects and synoptic evolution played only a secondary role in convective evolution after the convection outbreak.

Figure 3 presents the thermodynamic sounding used for model initialization. This profile is composited from the Cross-Chain Loran Atmospheric Sounding System (CLASS) sounding taken at the Fort Morgan Airport (located by the X in the 2202 UTC satellite photo in Figure 2a) at 2050 UTC

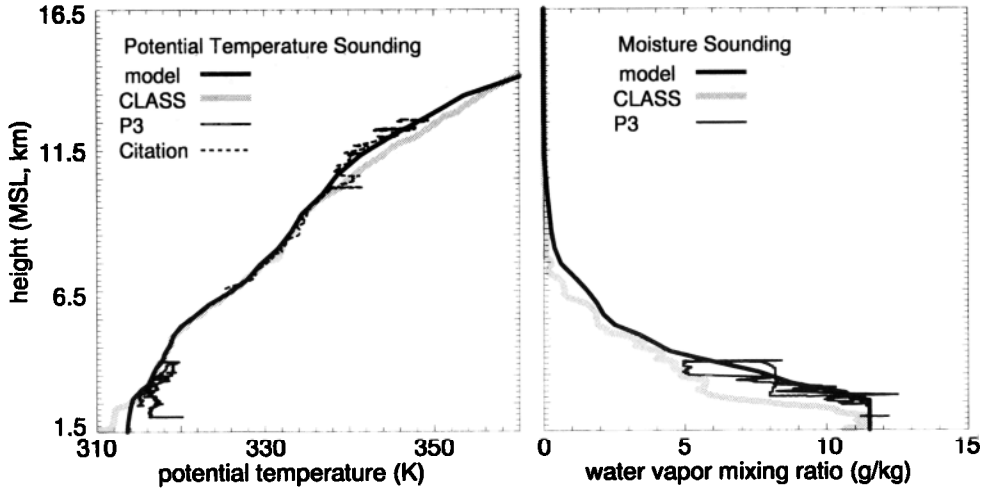

Figure 3. Thermodynamics sounding for the model environment, along with the CLASS sounding, P3 flight data from 2133:11 UTC to 2203:11 UTC, and Citation flight data from 2222:23 UTC to 2330:03 UTC.

on July 10, and P3 and Citation aircraft soundings (vertical profiles taken during ascent and descent during the event). The July 10 convection was deep (cloud tops $\geq$14 km mean sea level (msl)), and updrafts likely possessed vertical velocities greater than 30 m s^{-1} given the depth and strength of the reflectivity (see Figure 7) and the significant height that the overshooting tops extended above the tropopause [*Dye et al.*, 2000]. The CLASS sounding was located well to the south of the convective event and was likely not altogether representative of the convective environment. The Citation measurements indicate that the upper levels (~10 – 13.5 km msl) were significantly colder than found in the CLASS measurements. Also, the strength of the convection suggests that the boundary layer was somewhat warmer, as well as deeper, than the CLASS measurements, and is more consistent with the Citation and P3 measurements. Another difference between the CLASS and aircraft soundings is that the latter show no significant cap above the PBL, while the former has a strong one. Elevated heating along the Cheyenne Ridge may be responsible for this difference. The convective available potential energy (CAPE) in the composite model sounding is approximately 1850 m^2s^{-2}. Cloud base in the simulation using this sounding is at approximately 3.4 to 3.5 km msl, while cloud base was observed to be at approximately 3.6 km in the observations; the model vertical resolution is slightly over 200 m at cloud base, so the discrepancy is within the model error bounds.

The wind fields used in model initialization (Figure 4) are composited from the CLASS sounding and supplemented with data from the P3 and Citation. The turning of the winds seen at low levels, through the first 2.5 km above ground level (agl, ground level nominally at 1.5 km msl), was deduced in part from analyses of the P3's Doppler radar data. The strong shear located above the PBL is indicated in the aircraft data and Doppler analyses, and the strong shear in the PBL is indicated in the CLASS sounding. Given the

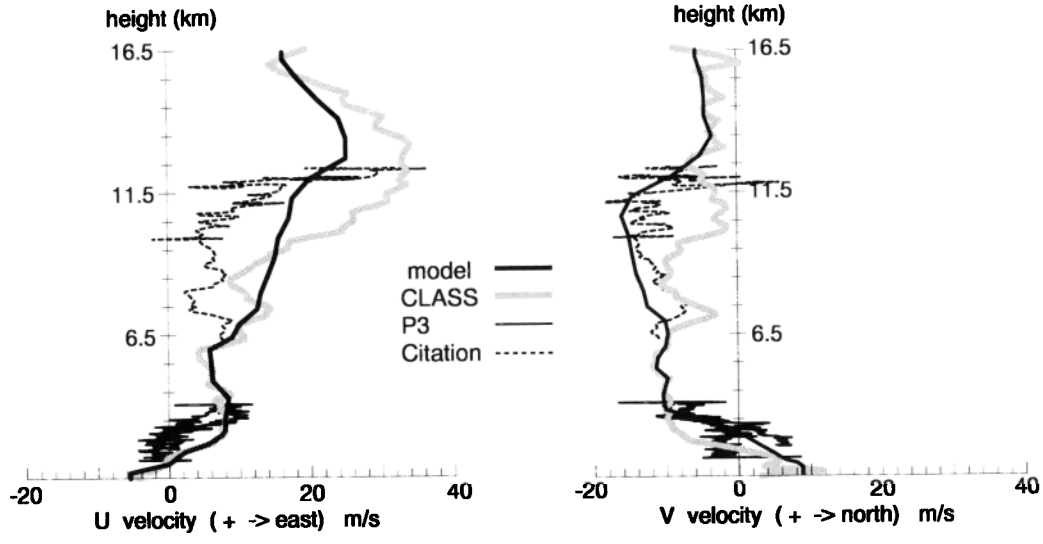

Figure 4. Environmental winds for the simulation, along with the CLASS sounding, P3 flight data from 2133:11 UTC to 2203:11 UTC,and Citation flight data from 2222:23 UTC to 2330:03 UTC.

lack of aircraft measurements in the boundary layer, we have used the CLASS sounding as a guide in retaining the strong shear in the upper part of the PBL. A thermodynamically well-mixed PBL possessing strong shear is not uncommon on the high plains (see, for example, the sounding and hodograph for the August 1, 1981, Miles City storm observed during Cooperative Convective Precipitation Experiment (CCOPE) [*Knupp*, 1987]).

Another important aspect of the wind profile is the height at which the upper level westerly jet appears. The CLASS sounding indicates that the strong westerlies begin at around 9.5 km msl, whereas the Citation measurements suggest that the strong westerlies begin a few kilometers above this. The anvil orientation between 9 and 11 km indicates that the winds were still predominantly from the northwest in this layer, an orientation consistent with the 0000 UTC, July 11

Table 1. Model Sounding

Height, m, msl	Pressure, mbar	Potential Temperature, K	Water Vapor, g kg^{-1}	U, m s^{-1}	V, m s^{-1}	CO, ppbv	O_3, ppbv
21,150	49.7	524.0	0.0	16.2	5.6	70	906
20,450	55.3	504.2	0.0	16.2	-5.6	70	846
19,750	61.7	484.4	0.0	16.2	-5.6	70	785
19,050	68.9	464.6	0.0	16.2	-5.6	70	724
18,350	77.0	445.1	0.0	16.2	-5.6	70	663
17,650	86.1	425.9	0.0	16.2	-5.6	70	603
16,950	96.5	406.3	0.0	16.2	-5.6	70	542
16,250	108.4	388.1	0.0	16.2	-5.6	70	484
15,550	121.7	378.0	0.0	18.4	-4.7	70	427
14,850	136.5	368.9	0.0	21.0	-4.4	70	370
14,150	153.0	360.4	0.0	24.0	-4.4	70	314
13,450	171.3	353.5	0.0	25.0	-3.4	70	257
12,750	191.3	349.5	0.0	25.0	-5.1	70	200
12,050	213.3	345.2	0.0	20.0	-9.0	70	162
11,350	237.3	341.4	0.0	17.0	-14.5	70	134
10,850	263.5	338.6	0.1	17.0	-16.0	71	112
9,950	291.8	336.8	0.1	15.5	-15.0	74	95
9,260	322.1	334.4	0.2	15.0	-14.5	76	78
8,605	352.9	333.1	0.3	14.0	-14.0	79	63
8,003	383.2	331.5	0.4	13.0	-13.0	84	50
7,447	412.9	329.4	0.6	12.5	-12.5	90	40
6,935	441.9	327.9	1.1	10.0	-10.0	90	37
6,463	470.1	325.8	1.6	9.0	-9.7	90	35
6,028	497.3	323.3	1.9	5.8	-10.0	95	40
5,627	523.5	321.7	2.1	6.0	-11.1	108	47
5,258	548.7	320.0	2.5	6.1	-11.3	105	55
4,917	572.7	319.1	3.4	6.2	-9.7	109	60
4,603	595.6	318.7	3.9	7.4	-10.1	113	60
4,314	617.2	318.1	4.5	8.4	-10.4	117	60
4,047	637.7	317.8	5.6	8.3	-10.3	120	60
3,802	657.0	317.1	6.6	8.1	-10.0	122	60
3,575	675.2	316.7	7.6	7.9	-7.2	125	60
3,367	692.3	316.4	8.2	7.9	-3.3	128	60
3,174	708.3	316.1	8.8	7.9	-2.2	130	60
2,997	723.3	315.3	9.6	7.3	0.0	132	60
2,834	737.4	314.8	10.6	6.4	1.1	134	60
2,683	750.6	314.3	10.9	5.4	2.1	135	60
2,544	762.8	314.1	11.5	3.7	3.0	135	60
2,416	774.3	314.0	11.5	2.2	3.9	135	60
2,298	784.9	313.9	11.5	1.5	4.7	135	60
2,190	794.9	313.9	11.5	1.0	5.4	135	60
2,090	804.1	313.8	11.5	0.5	6.0	135	60
1,997	812.7	313.8	11.5	-0.1	6.8	135	60
1,912	820.6	313.7	11.5	-1.6	8.2	135	60
1,834	828.0	313.7	11.5	-3.1	8.6	135	60
1,762	834.9	313.7	11.5	-4.4	9.0	135	60
1,695	841.2	313.6	11.5	-5.5	9.0	135	60
1,634	847.1	313.6	11.5	-5.5	9.0	135	60
1,577	852.5	313.6	11.5	-5.5	9.0	135	60
1,525	857.6	313.6	11.5	-5.5	9.0	135	60

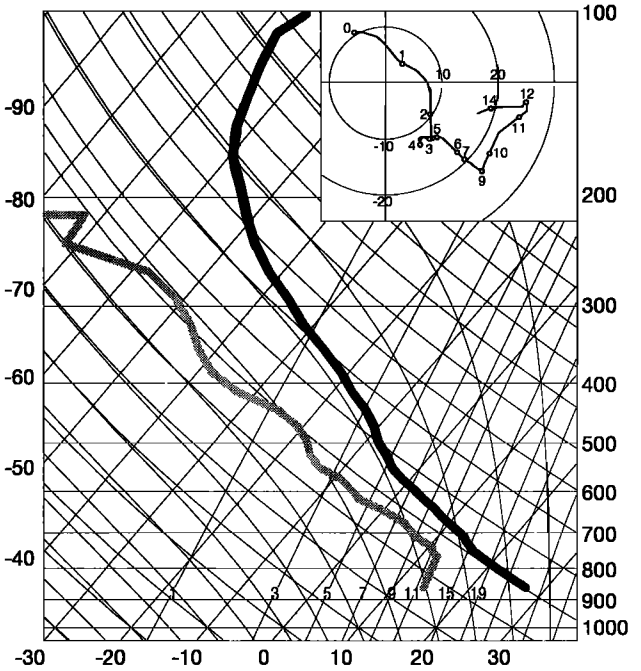

Figure 5. Model sounding plotted on a skew-T diagram along with the hodograph. The hodograph heights are in kilometers above the ground (msl minus 1.5 km). The thermodynamic sounding has a maximum CAPE of 1850 $m^2 s^{-2}$ and a bulk Richardson number of approximately 7 (computed using 500 m and 6 km winds).

sounding from Scottsbluff, Nebraska (not shown), and not consistent with the CLASS sounding. It appears that the shortwave trough discussed in section 2 was responsible for the shift from westerlies to northwesterlies in this layer, as it had passed through the area by this time. The model initial wind profile thus largely follows the Citation data and the Scottsbluff sounding in setting the height of the westerly jet. The amplitude of the jet is set by matching the P3 retrieved winds with the simulated winds at the jet level.

The full sounding used to initialize the model, along with the skew-T plot of the sounding and the hodograph, is given in Table 1 and Figure 5. The simulation has a horizontal resolution of $\Delta x = \Delta y = 1$ km. The vertical resolution provides 50 levels from the surface to the model top, with resolution varying from 50 m at the surface expanding to 700 m at 10 km agl. The model domain size is $120 \times 120 \times 20$ km. Convection is initiated by placing three positively buoyant thermals aligned NW-SE and spaced approximately 20 km apart. The analytic form of the thermals is

$$\theta' = \frac{\Delta\theta}{2}(\cos(\pi r) + 1) \qquad r < 1,$$

where

$$r = \left[\left(\frac{x - x_o}{x_r}\right)^2 + \left(\frac{y - y_o}{y_r}\right)^2 + \left(\frac{z - z_o}{z_r}\right)^2\right]^{1/2},$$

$x_r = y_r = 10$ km, $z_r = z_o = 1500$ m, and $\Delta\theta = 3$K. In the multicellular stage of the observed system, the line orientation was NW-SE, and the line was composed of two to four active cells with a total line length varying between 30 to 70 km (see the 4.5 km msl dBZ fields in Figure 6 at 2312 and 0005 UTC). The initialization using the above described thermals produces a line of three cells 30–60 min into the simulation. These cells are similar to the system elements as observed between approximately 2300 and 2400 UTC. We have specified the initial line orientation in the simulation, but notably the line does not reorient itself as new cells are generated, and the simulated convection maintains the correct line orientation during the multicellular regime. The convection transitions into a supercell a little after 2 hours into the simulation, while the observed system transitioned to a supercell after about 0100 UTC on July 11, or about 3 hours into the event.

The types of convection observed are what would be expected in the given environment. That is, given the initial potential instability and vertical wind shear, convective storm theory suggests that isolated cells and supercells are likely [*Weisman and Klemp*, 1982]. Thus the convective evolution from isolated cells to a supercell is understandable. Moreover, the supercell's southward movement and the observed cyclonic rotation in the mesocyclone are also expected, given the clockwise curvature in the low-level hodograph.

4. Comparison With Observations

The structure of the July 10 STERAO convective system is most easily appreciated by examining horizontal and vertical cross sections of radar reflectivity and Doppler-derived horizontal wind fields. Figure 6 presents horizontal cross sections of radar reflectivity at 4.5 km and 10.5 km msl for the observed system at 2312 UTC on July 10 and 0005 UTC and 0128 UTC on July 11. Included for comparison are model reflectivity cross sections at analogous times, derived from the simulated hydrometeor distributions. The earliest comparison time (2312 UTC, July 10) corresponds to the linear stage of the convective system; at this time the line was multicellular with cells oriented along a NW–SE axis. The second comparison time (0005 UTC, July 11) is shortly before the convection's transition to a supercell, and the last comparison time (0128 UTC, July 11) reflects the supercellular stage.

The reflectivity patterns in the observed and simulated convective systems are generally similar at each time shown, although they differ in many details. The simulation reproduces the NW–SE orientation of the line of cells at the early and middle times. The model and observed reflectivity maxima compare well, with the observations showing slightly higher reflectivity maxima in the upper level cross sections. At the lower and upper levels, both the observed and simulated systems display significantly tighter reflectivity gradients on the system's southwestern side compared with the northeastern side. These patterns are due to the westerly flow at upper levels stretching the anvil outflow and precipitation pattern eastward. In both observation and the model, discernible fingers of higher reflectivity can be seen extending eastward from the active cells. Generally, the higher-reflectivity patterns (area > 40 dBZ) are similar

in size, while the lowest reflectivities are smaller in size in the simulations compared with the observations. This discrepancy may be caused by deficiencies in the bulk microphysical parameterization used in the model, or possibly erroneously low values of moisture at upper levels used in the model sounding that would lead to excessive evaporation in the anvil. The discrepancy could also be caused by by differences in the updraft mass flux.

The observed system transitions to a supercell after about 0100 UTC on July 11, or after a little more than 3 hours of active convection along the line. The simulated convection transitions to a supercell after approximately 2 hours in the simulation. The structure in the reflectivity fields is similar in both cases, with the anvil extending to the southeast and then turning more eastward at greater distances from the convective updraft, with this pattern being somewhat more pronounced in the simulation. While the appearance of the supercell follows a buildup of the surface cold pool in the simulated system, surface observations are lacking to document whether the buildup of the cold pool was the critical factor for the observed supercell's development. For the simulated storm a strong cold pool was necessary in this environment for producing an appropriately tilted, quasi-steady updraft. The observed system decayed by 0230 UTC (2030

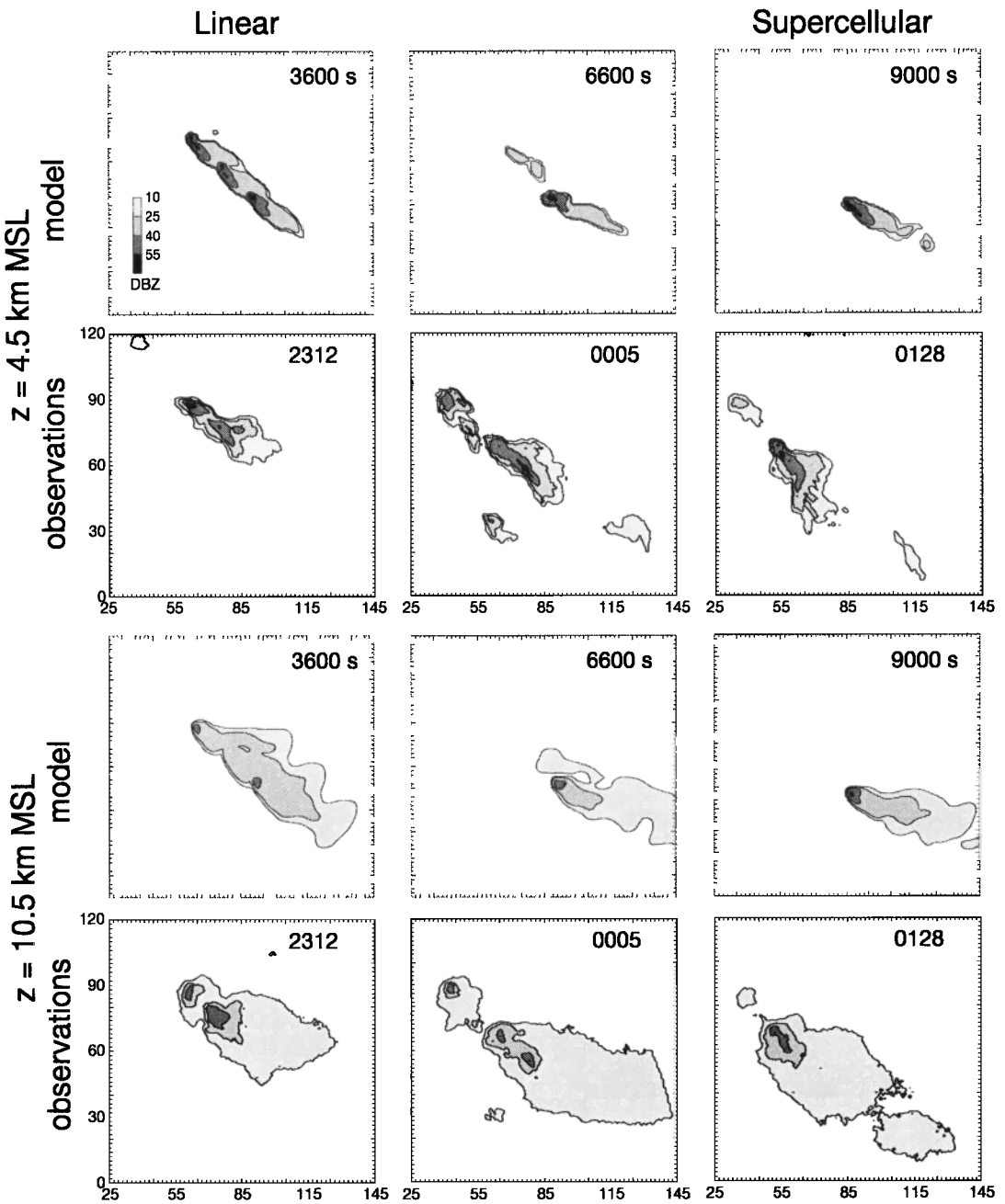

Figure 6. Horizontal cross sections of radar reflectivity from the CHILL radar and derived from the simulation. The horizontal and vertical axes are distance east and north from CHILL radar (kilometers), respectively.

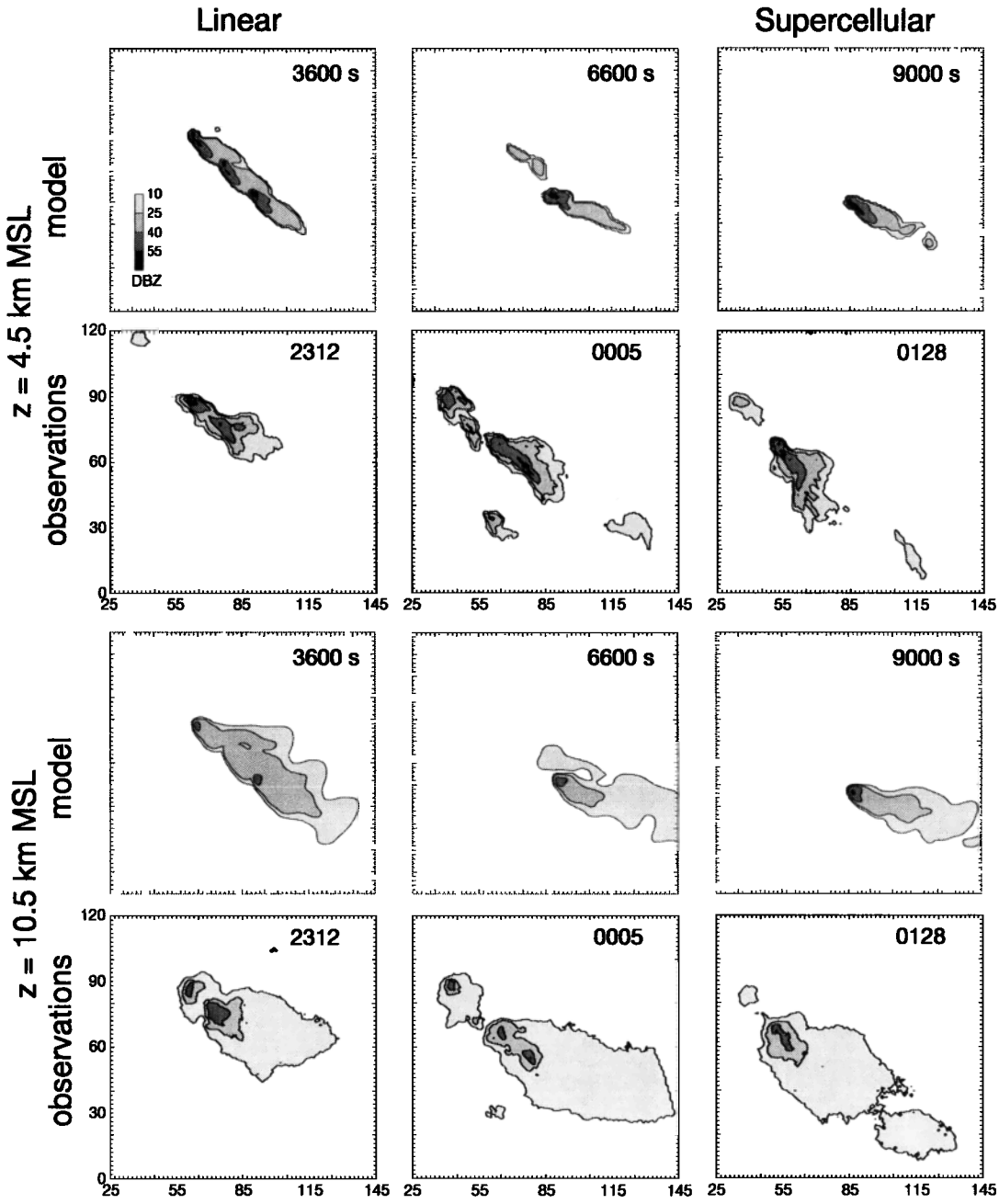

Figure 6. (continued)

local time, MDT). Nocturnal cooling of the boundary layer, a likely cause of the decay of the observed system, is not accounted for in the model.

Vertical cross sections through the observed and simulated systems are shown in Figure 7 for both the multicellular and supercell stages. The height of the convective elements and the depth and horizontal extent of the anvils are similar. The simulated cells are comparable in depth to most cells observed in the multicellular stage (e.g., the NW cell (leftmost) at 2312 UTC), although they are substantially shallower than the deepest observed cell (the rightmost cell at 2312 UTC). At later times the simulated supercell is substantially deeper than the observed supercell. The tops of the observed convective cells are fairly high, with 35 dBZ echoes extending above 14 km msl for the strongest cells in the 2300 to 2400 UTC time period. The anvil top decreases in height with increasing distance downwind of the updrafts in both the observations and the simulation. This behavior likely reflects both dynamical and microphysical effects: the overshooting of convective tops and subsequent parcel descent, followed by evaporation of hydrometeors and cooling (and further descent) of anvil air as it flows outward. In the simulation the upper anvil boundary is also the upper boundary of the CO (tracer) plume, and thus the air is generally descending. Analyses of cross sections through the anvil away from the active cells show that the hydrometeor and dBZ maxima do not correspond to the CO (tracer) plume maxima. Thus hydrometeor sedimentation in the anvil also

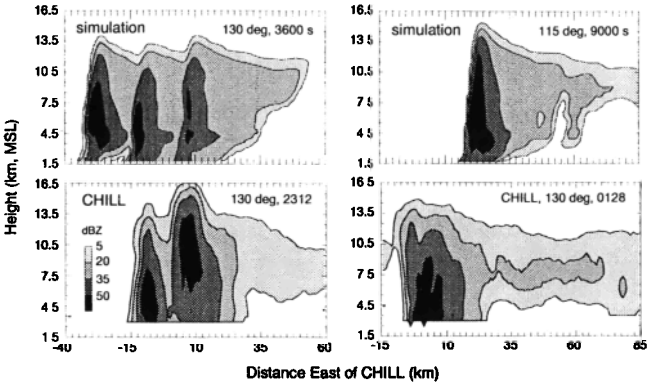

Figure 7. Vertical cross sections of radar reflectivity from CHILL and reflectivity derived from the simulation.

lowers the height of the dBZ maximum in the anvil (the dBZ maximum implies significant sedimentation rates), but sedimentation does not directly cause the air parcels to descend.

Doppler analyses of reflectivity and horizontal wind fields were produced using data from the P3 airborne Doppler [*Jorgenson et al.*, 1996] and Colorado State University (CSU) University of Chicago/Illinois Water Survey (CHILL) radar. Figure 8 shows horizontal cross sections from the analyses and from an analogous time in the simulation at four heights. Low-level cross sections at 2400 m, 2900 m, and 3900 m msl show the turning of the wind with height at low levels (in and above the boundary layer). The areal extent of the reflectivity pattern is limited at low levels, and the environmental winds are best estimated from winds at the southeastern edge of the reflecting region where anvil precipitation produces a signal away from the active convection. The CLASS sounding indicated that environmental winds turned to westerlies and northwesterlies at significantly lower altitudes in the boundary layer than suggested in the Doppler analyses. The Doppler analyses are consistent over time, and show that the low-level hodograph changed little over the lifetime of active convection.

Upper level reflectivity and horizontal winds at 11.4 km msl are also depicted in Figure 8. The retrievals show that the winds remain northwesterly at 11.4 km, while they have shifted to predominately westerlies at 12.4 km (not shown). Although the CLASS sounding suggested that the shift to westerlies occurred by 10.4 km msl, simulations with the CLASS winds produced east-west oriented anvils rather than the NW-SE orientation observed.

5. Tracer Transport

CO and O_3 are included as passive tracers in the simulations to examine the effect of the convection on the distribution of species. Initial model soundings of CO and O_3 are given in Figure 9, where they are superposed over scatterplots of CO and O_3 measured outside of the cloud by the P3 and Citation aircraft for the entire flights. The highest concentrations of CO (> 135 ppbv) in the model profile are found in the boundary layer, with concentrations decreasing up to the midtroposphere where a background value of approximately 70 ppbv is reached. The O_3 profile is essentially an inverse of the CO profile, with low concentrations and little vertical variation throughout most of the lower troposphere, and increasing values and strong gradients as the lower stratosphere is encountered. The O_3 profile differs substantially from the climatological profile for Boulder, Colorado, in July [from *Logan*, 1999] which is also plotted in Figure 9. O_3 concentrations in the simulation profile are generally slightly more than a standard deviation higher than the observed climatological values in the upper troposphere below the tropopause (approximately 13.5 km msl). The out-of-cloud observed O_3 concentrations vary widely in the region just below the tropopause. The higher values observed at 12.5 km msl are found on the southwest side of the storm, and the lower values correspond to observations on the northeast side of the storm. We have constructed the O_3 sounding to reflect the lower observed values, which are also closer to the climatological values. The high out-of-cloud values on the southwest side of the storm below the tropopause could indicate convectively induced strong subsidence and tropopause folding outside the storm around the anvil. Our convective simulation does not produce strong tropopause subsidence or folding in the vicinity of the anvil.

5.1. Tracer Distributions and Comparison With Observations

Figure 10 presents horizontal and vertical cross sections of CO for two times: during the linear convective stage at 1 hour into the simulation and during the supercell stage at 2.5 hours into the simulation. CO values significantly above 100 ppbv extend well into the anvil at an altitude of 11.5 km msl. Citation passes in the anvil around this level [*Dye et al.*, 2000, Figure 9], (at 2312–2320 UTC at ~11.6 km msl and at 2331–2339 UTC at ~11.2 km msl) have peaks of approximately 110 ppbv with typical in-cloud values of 90 to 100 ppbv. The Citation cross sections were taken approximately 40 to 50 km downwind of active convective cells during the linear stage of the system's evolution. Values in excess of 95 ppbv are found well downwind in the simulations (see the horizontal cross sections in Figure 10). At 3600 s into the simulation the anvil is still expanding and is just reaching 50 km downwind of the convectively active region. The higher concentrations of CO in the linear stage tend to be at or below 11.5 km msl in both the simulations and the observations (see the later Citation passes as given by *Dye et al.*, [2000, Figure 9]), although this behavior is more pronounced in the observations.

The CO cross sections at 3600 s can be compared with convective system simulations from *Pickering et al.* [1992b], where modeling results for CO transport in the June 10-11, 1985, Preliminary Regional Experiment for Stormscale Operational and Research Meteorology (PRESTORM) convective system and the 26 April 26, 1987, ABLE2B system are given. Dilution of boundary layer air detrained into the anvil is evident in both of these linear convective systems and in the STERAO system, but boundary layer concentrations are not found in the anvils. Thus some dilution (entrainment) of boundary layer air must have occurred in the updrafts.

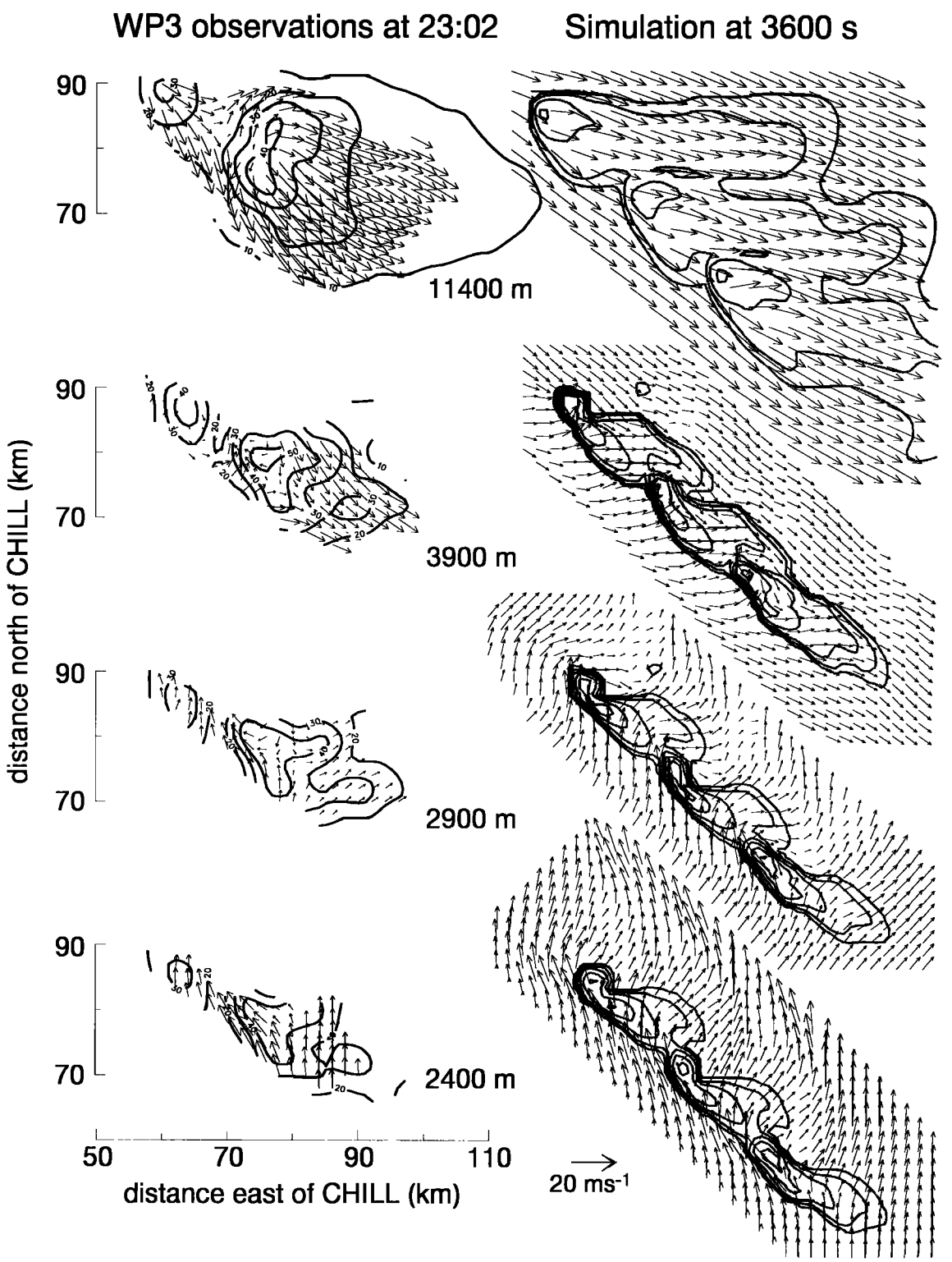

Figure 8. Horizontal cross sections of radar reflectivity and storm relative horizontal velocities (the storm speed $(u,v) = (1.5,-5.5)$ m s^{-1}) from the P3 Doppler radar and from the simulation in the system's multicellular stage. Heights are msl and the reflectivity contour interval is 10 dBZ.

The simulated STERAO supercell can be compared with the 3-D simulations of *Hauf et al.* [1995] for the July 21, 1992, Cloud Experiment Oberpfaffenhofen and Transports (CLEOPATRA) storms. Hauf et al.'s simulated supercells showed almost undiluted boundary layer air reaching the anvil (based on O_3 concentrations), conditions also found in the supercell stage of the simulated STERAO storm (Figure 10). Although *Hauf et al.* [1995] only examined the simulation results in the anvil region close to the updraft, they argued from observations that undiluted air may be found over

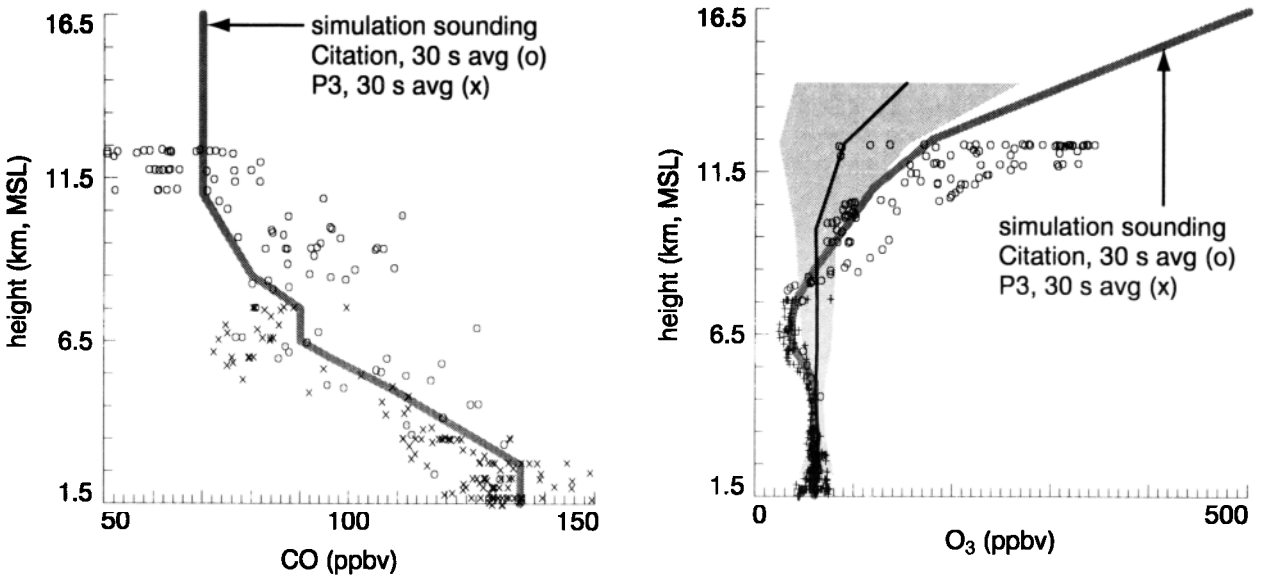

Figure 9. CO and O_3 soundings for the simulation along with out-of-cloud CO and O_3 measurements from the P3 and Citation aircraft. The climatological sounding for July in Boulder, Colorado, is also plotted [from *Logan*, 1999] with the shaded area outlining the ± 1 standard deviation values.

100 km downwind in the anvil in the CLEOPATRA storms. In contrast, the STERAO simulation does not show undiluted boundary layer air far downwind in the anvil.

Figure 10 also presents O_3 cross sections from the simulations at 3600 s. One observed feature which is not reproduced by the simulations is the difference between the southwest and northeast out-of-cloud O_3 values. The observations show elevated O_3 values (compared to the background values) on the SW side of the anvil [*Dye et al.*, 2000, Figure 9] (see Citation passes at 11.2 km, 11.6 km, and 11.8 km msl; the out-of-cloud values vary by 50 ppbv). The simulation's vertical cross section of O_3, which includes an outline of the 1 dBZ reflectivity, shows that the air outside the anvil-cloud region is essentially that reflected in the original model profile. There is no pronounced subsidence on the southwest side of the anvil in the simulation that would explain the high values for observed O_3.

Flight track data can be directly compared with simulation data by superposing the flight data with similar tracks taken through the simulation fields. Figure 11 presents CO and O_3 measurements for Citation passes 2 and 5 (see *Dye et al.* [2000] for the track locations) along with similar passes through the simulation (approximately 10 and 50 km downwind of the southeasternmost cell, with a SW-NE and N-S orientation, with half an hour spacing between the passes). Given the observed anvil winds, these passes are sampling approximately the same air parcels as they flow through the anvil. For CO the peak values and fluctuation are similar in the observations and model, and both show a decrease of between 5 and 10 ppbv between the upstream and downstream values, suggesting a small amount of entrainment and mixing occurred. The O_3 measurements are similarly in agreement in the early pass, although the simulations suggest more mixing occurs as the air progresses downwind in the anvil; the observations maintain a broad O_3 minimum with values similar to the upwind pass, while the model shows a significantly narrower minimum, also with values similar to the earlier pass. As noted in the discussion of the horizontal cross sections, the asymmetry observed in O_3 from the SW to NE side of the system is not captured in the simulation. *Stenchikov et al.* [1996] found such an asymmetry in their 2-D simulations of the June 28, 1989, North Dakota Thunderstorm Project storm, and attributed the asymmetry to strong downward tropopause deformation on the upwind side of the anvil; there were no observations to verify the existence of the asymmetry for that storm.

5.2. Vertical Tracer Fluxes

The conservation equation for the passive tracer species can be expressed as

$$\frac{\partial(\bar{\rho}\phi)}{\partial t} = -\frac{\partial(\bar{\rho}u\phi)}{\partial x} - \frac{\partial(\bar{\rho}v\phi)}{\partial y} - \frac{\partial(\bar{\rho}w\phi)}{\partial z}, \qquad (1)$$

where ϕ is the mixing ratio of the tracer. A general measure of the convective vertical transport can be obtained by horizontally integrating (1) over the domain.

$$\frac{\partial}{\partial t}\int_{\Omega}(\bar{\rho}\phi)\,\partial\Omega = -\int_{\Omega}\frac{\partial(\bar{\rho}w\phi)}{\partial z}\,\partial\Omega - \int_{\Gamma}(\bar{\rho}u_{\mathrm{n}}\phi)\,\partial\Gamma. \qquad (2)$$

This equation provides the instantaneous change in the mass of tracer ϕ at a height z, horizontally integrated over the domain Ω with spatial boundaries Γ and boundary-normal velocity u_{n}. The last term on the right-hand side of (2) is the net flux through the boundaries. Having computed all the terms in (2) for CO and O_3 at each time step, we find that this term is always much smaller than the other two and can be ignored. The first term on the right-hand side of (2) is the horizontally integrated vertical flux divergence, and it is the dominant term in the horizontally integrated time rate of change of $\bar{\rho}\phi$.

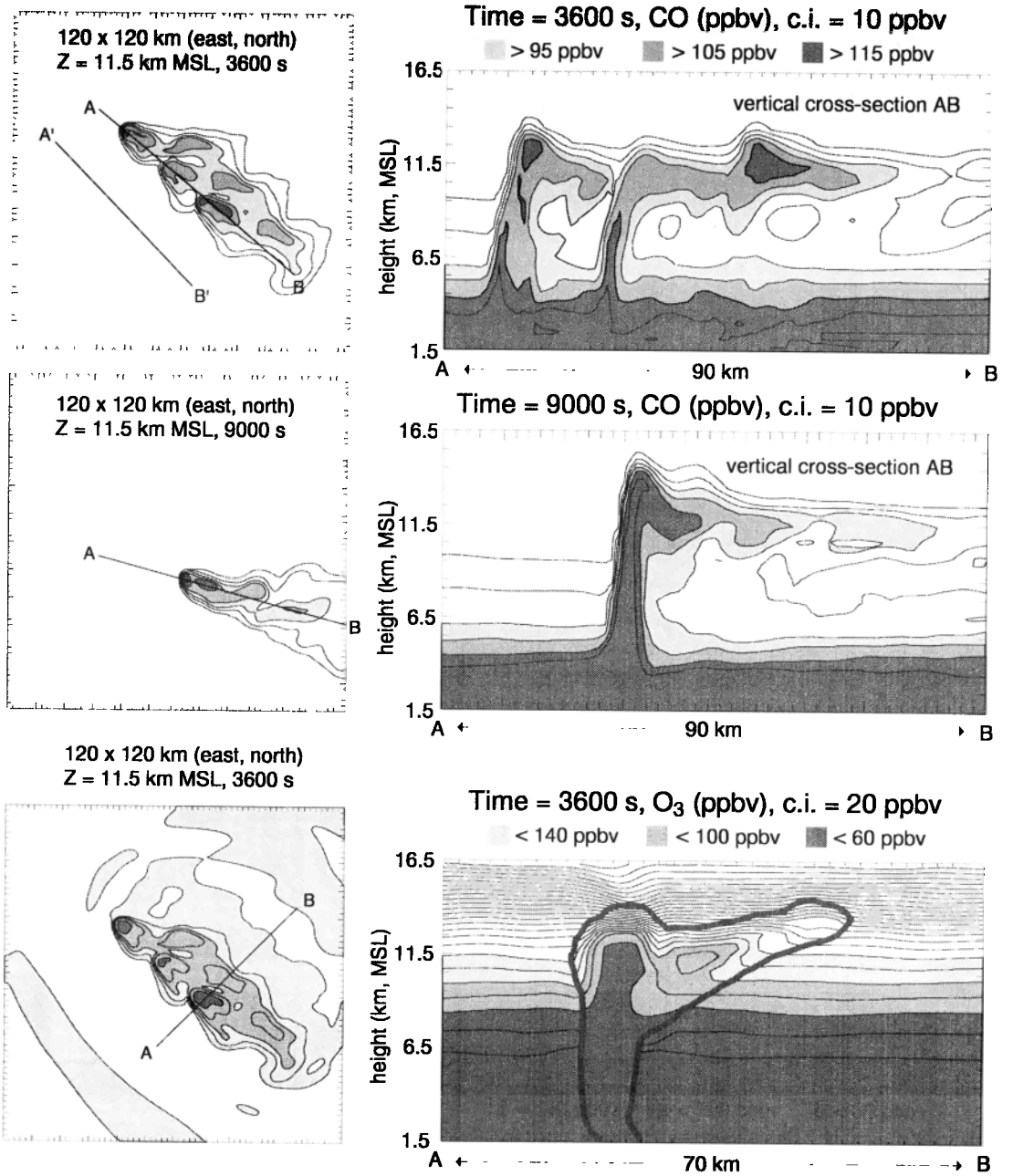

Figure 10. Horizontal and vertical cross sections of CO at 3600 s and 9000 s, and O_3 at 3600 s. The cloud field is outlined in the O_3 vertical cross section. Contour intervals (c.i.) are as noted in each cross section.

Equation (2) can be time integrated to reveal the net change in the tracer ϕ as a function of height (kg m^{-1}) through time t,

$$\int_0^t \int_\Omega \frac{\partial}{\partial z}(\bar{\rho} w \phi)\, \partial\Omega\, \partial t. \tag{3}$$

For the tracer CO this quantity (3) is depicted in Figure 12. This integrated flux divergence has a similar profile for the three times plotted. There is a net gain in CO in the atmosphere at almost all heights above approximately 8 km msl, and a corresponding net decrease below this level, although the flux divergence is not uniformly negative here, particularly at the final time. Above 8 km msl, the maximum time-integrated flux divergence increases with altitude, indicative of deepening convective transport as the system becomes supercellular.

The time-integrated vertical flux divergence of CO calculated here can be compared qualitatively to the passive tracer redistributions computed by *Pickering et al.* [1992a, Figure 2] for the August 3, 1992, ABLE2B convective system. In both systems there is only a small amount of detrainment at midlevels (from about 5 to 8 km msl in the STERAO case and from about 5 to 9 km msl in the ABLE2B case), with the bulk of the detrainment occurring in the anvil region. Boundary layer concentrations are reduced by system-scale subsi-

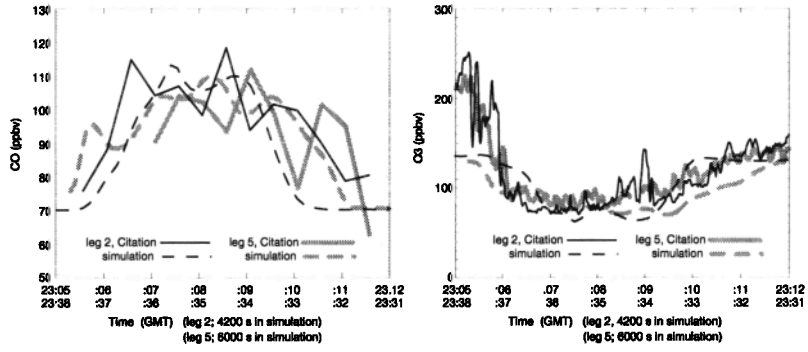

Figure 11. Citation CO and O_3 measurements for anvil passes close to the southeasternmost convective cell (leg 2, 10 km downwind, 11.6 km msl) and downwind (leg 5, 50 km downwind, 11.2 km msl), along with analogous tracks taken through the simulation. The plot tracks are from the southwest (left) to the northeast (right).

dence and transport in convective downdrafts. The structure in the STERAO CO flux divergence arises in part because of the structure of the initial CO profile, which presents a significant vertical gradient of CO between 3 and 8 km msl.

The net mass of CO injected into the upper troposphere and lower stratosphere can be computed by vertically integrating the flux divergence (3) over the desired layer. Figure 13 is a plot of the time integral of the vertically integrated flux divergence (from z= 8 to 15 km msl) during the 3 hour simulation, along with the instantaneous rate of change of the net flux in this layer. While the net mass of CO added to this layer increases monotonically, the rate of increase is not constant. After convection is established (after 1/2 hour) peaks in the net flux are followed by a minimum in the flux that is less than a third of the peaks. This minimum is followed by a steady increase. Examination of the instantaneous vertically integrated flux associated with positive and negative vertical velocities shows that the minimum in flux divergence at approximately 1.5 hours is caused primarily by a weakening of the updraft transport, not by a strengthening of the downdraft transport. Also of interest is the result that the final peak (at 3 hours) is at least half as large as the earlier peaks (at ~1 hour), even though at 3 hours the vertical transport is being performed by a single cell as opposed to three or four cells. The significantly enhanced transport associated with a supercell is also indicated in Figure 10, where the vertical cross section at 9000 s shows a broad, deep updraft containing high levels of CO (> 115 ppbv). In contrast, at the earlier time (3600 s) the updrafts are significantly narrower and somewhat shallower, and the maximum values of CO are somewhat lower, particularly at higher levels.

The net CO deposition into the anvil can be compared qualitatively with the monthly mean convective mass flux of CO out of the boundary layer computed by *Thompson et al.* [1994] for the central United States for the month of June. For the box bounded by 40° – 42.5°N latitude and 102.5°–105°W longitude, Thompson et al. estimated that 11–17.8 $\times 10^7$ kg of CO per month is fluxed out of the boundary layer, and 7.89–9.95 $\times 10^7$ kg of CO per month is fluxed into the boundary layer, for a net flux of CO per month ranging from a minimum of 11 – 9.95= ~1 $\times 10^7$ kg to a maximum of 17.8 – 7.89= ~9.9 $\times 10^7$ kg. The simulated STERAO storm produced a net flux of 2.5 $\times 10^5$ kg of CO over the 3 hour simulation. Given that the observed convective system lasted a bit over 4 hours, and extrapolating the CO flux in the simulation, one might expect a flux of around 5 $\times 10^5$ kg of CO over the storm's lifetime. If one assumes that the net flux out of the boundary layer is mostly deposited into the anvil, then between 20 and 200 storms of this type per month would be required within this region to produce the minimum and maximum net flux estimated by Thompson et al. The lower limit for the number of storms, and hence for the flux estimated by Thompson et al., appears to be the more reasonable estimate.

5.3. Parcel Trajectories

Trajectories are calculated in the model to identify the sources of convective updraft and anvil air. The trajectory calculations are performed as the Eulerian model is inte-

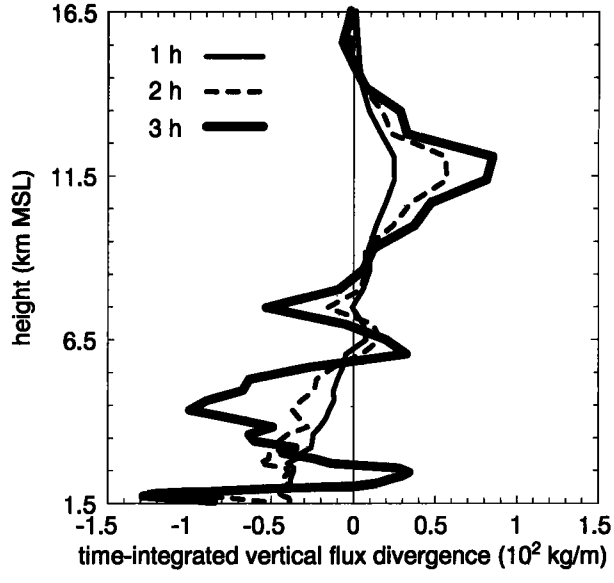

Figure 12. Time-integrated flux divergence for CO (equation (3)) at 1, 2, and 3 hours.

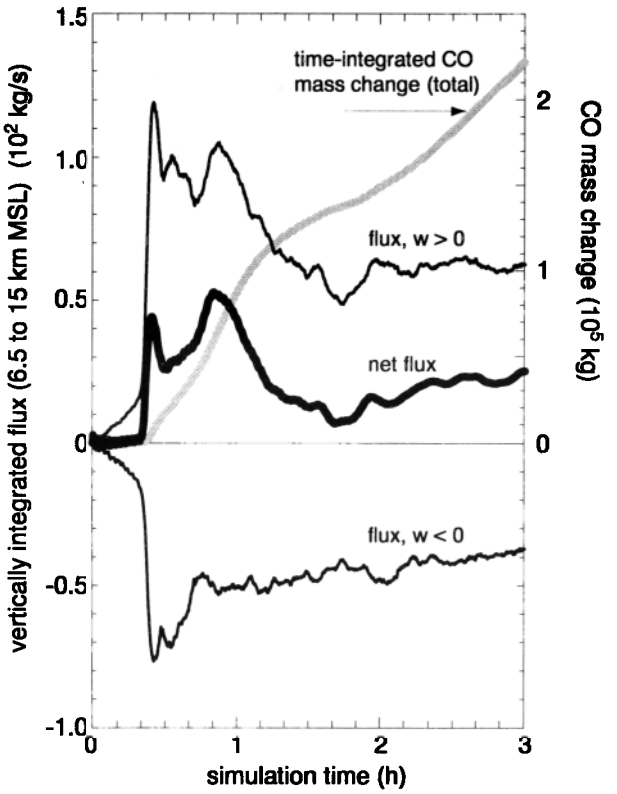

Figure 13. Vertical flux divergence for CO integrated from 8 to 15 km msl. Instantaneous values are indicated on the left axis, and the time integrated net flux is indicated on the right axis.

grated, and parcel positions are updated every time step using a second-order time integration scheme coupled with a tri-cubic/monotonic spatial interpolation scheme. Using these forward trajectories, parcels are released and their paths are examined.

Figure 14 shows the maximum heights reached by parcels released from the lowest 4 km above the surface (1.5 to 5.5 km msl) along the cross section $A'B'$ (shown in the upper left hand diagram of Figure 10). The parcels are released at 30 min in the simulation, and parcels reaching the convective updrafts do so between 70 and 90 min. The delineation between low-level parcels that do or do not reach their level of free convection is striking, and the separate bands in Figure 14 identify parcels destined for two different updrafts. Note that parcels in the lowest levels, from 1.5 to 2.0 km msl (0 to 0.5 km above the surface) do not reach their level of free convection. The low-level air being ingested by the convective updrafts instead originates from a layer beginning at approximately 2 km msl and extending to a little less than 3.5 km msl.

Significant curvature in the hodograph was observed in the lowest 2 km with winds veering from southeasterly at 1.5 km msl (the surface) to northwesterly at 3.5 km msl. The hodograph curvature is responsible for the tilted structure seen in Figure 14; air at 3.5 km msl is traveling to the east, while air at 2 km msl is traveling to the north. Selected trajectories of updraft parcels plotted in a ground relative framework are depicted in Figure 15. The results further emphasize the flow branches: Parcels originating from around 3.5 km msl come from the west, parcels from around 2.5 km msl come from the southwest, and parcels from around 2.2 km msl come from the south, while parcels starting below 2 km msl do not enter the updrafts. Thus the boundary layer air that is ultimately carried into the anvil originates predominately from west and southwest of the storm (rural/urban to the west with metropolitan Denver to the southwest) as opposed to south and southeast of the storm (largely agricultural areas). This pattern remains largely unchanged over time, and trajectories started at later times indicate that air in the lowest 500 m is never entrained into the convective updrafts, even during the supercellular stage.

The P3 aircraft measurements indicate both along-line (horizontal) gradients of chemical species at low levels away from the system (SW of the convection, likely in parts of the inflow), and significant vertical gradients [see *Dye et al.*, 2000, Plate 3]. Thus the characterization of some chemical species' inflow can be difficult given the 3-D structure of the inflow. Unfortunately, the observations are inadequate to document this inflow structure, particularly with respect to the lack of inflow in the 0–500 m layer in the simulation. A further note of caution is appropriate. We find that the depth of inflow air in the simulation (i.e., the air entering the updrafts and exiting via the anvil) is sensitive to details in the boundary layer formulation, the microphysical parameterizations, and the low-level thermodynamic sounding and hodograph used. While the observations may not be adequate for confirming the simulated features, the lack of inflow from the lowest levels in the PBL may be common in weakly forced convective systems that do not develop strong, deep cold pools. Indeed, this may be very common on the high plains of the central United States, where high

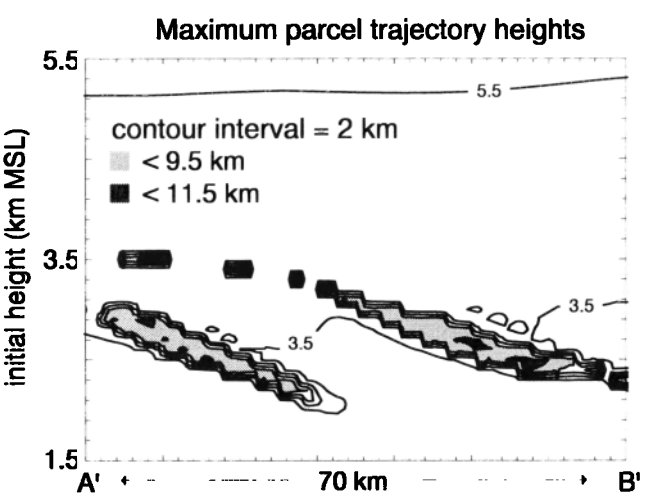

Figure 14. Maximum heights obtained by parcels released on the vertical cross section A'B' (see Figure 10) at 1/2 hour, contoured relative to their initial position. A total of 8080 parcels trajectories were calculated, and the initial parcel spacing is uniform at 700 m horizontally and 50 m vertically. The contour interval is 2 km starting at 3.5 km msl.

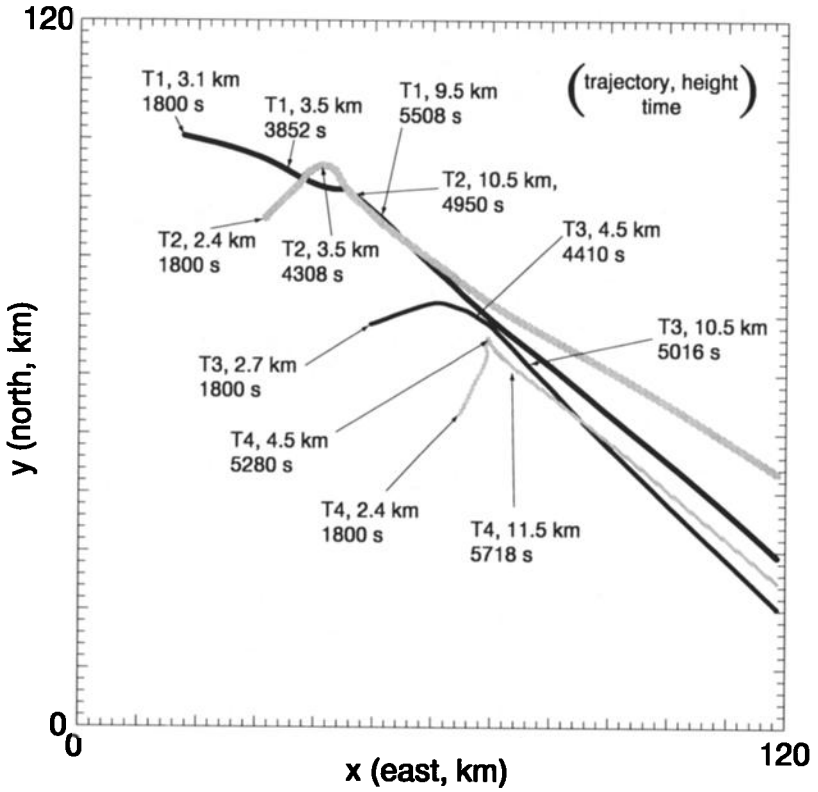

Figure 15. Selected parcel trajectories plotted in a ground relative framework. Heights are given in msl (ground level is 1.5 km msl).

cloud bases and weak cold pools are common in summertime convection.

The trajectories plotted in Figure 15 give an indication of parcel residence time in updrafts. For example, trajectory 1 ascends rather slowly, with nearly 1/2 hour spent in the updraft, while trajectories 2, 3, and 4 ascend much more quickly, with approximately 10 min spent in the updraft. The histogram of times spent in the updraft, given in Figure 16, provides a more quantitative measure of parcels' updraft residence times. Residence time in the updraft is defined here as the time necessary for a parcel to travel from 4 km msl (2.5 km above the surface, where it is entering the updraft) to 500 m below its maximum attained height. Only those parcels ascending above 8 km msl are considered and we are using the data from the trajectory analysis in Figure 14. Most parcels spend between 10 and 20 min in the strong updrafts, although there is a significant tail out past 30 min. With a mean maximum height of around 11 km msl, the average vertical velocity of a parcel that takes 10 min to ascend would be approximately 10.8 m s^{-1}. Although significantly higher instantaneous vertical velocities occur (in the simulation, maximum vertical velocities average around 30 m s^{-1}), parcels do not spend most of their time in the strongest updrafts.

Trajectories beginning at upper levels (above the PBL) show that downdrafts tend to be shallow; rarely do air parcels descend much more than 3 km in the downdrafts. Thus air deposited into the boundary layer by convective downdrafts has its source only a few kilometers above the boundary layer. Also, upper tropospheric and lower stratospheric air does not descend far in the downdrafts; the deeper downdrafts tend to originate anywhere from 4.5 to 7.5 km msl, not from higher in the troposphere. These results are consistent with the earlier findings of *Knupp* [1987], that the maximum heights of low-level downdrafts reaching the PBL appear to be at the transition level where the environmental temperature profile turns absolutely stable. In the model sounding

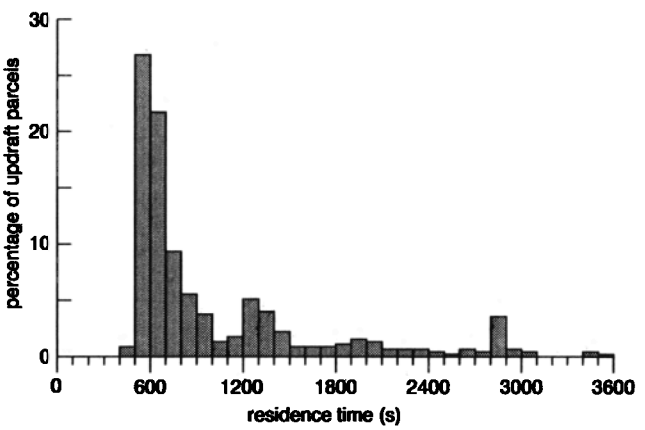

Figure 16. Histogram of parcel residence times in the updrafts. Residence time is defined as the time it takes a parcel to rise from 4 km msl (2.5 km agl) to 500 m below the maximum altitude obtained along the trajectory.

(Figure 5) this transition level is at approximately 550 mbar or a little less than 5.5 km msl (4 km agl).

6. Summary

The three-dimensional structure and evolution observed in the July 10, 1996, STERAO convective system has been broadly reproduced within a nonhydrostatic cloud model simulation using an idealized horizontally homogeneous sounding and no terrain. The simulated convective system captures the evolution of the multicellular line to a supercell. Line orientation, anvil structure, horizontal wind fields, depth of convection, and derived radar reflectivity compare well with observations. The success of the simulation suggests that the synoptic evolution and terrain effects acted to precondition the environment and perhaps initially force the convection, but played only a secondary role in the system evolution.

Simulated passive tracer transport of CO and ozone yields results generally in agreement with aircraft measurements, although the simulation does not reproduce the high values of ozone observed on the southwest side of the anvil. In the simulated system, CO transport from the boundary layer to the anvils shows a small amount of entrainment of environmental air in the updrafts, followed by a similarly small amount of dilution occurring with transport downwind in the anvil. Entrainment and dilution in the simulation are less obvious at later times, that is, during the supercell phase, than during the earlier multicellular phase.

Analyses of the vertical flux divergence for CO in the simulation show a net gain at almost all levels above 8 km msl (middle to upper troposphere and lower stratosphere). The rate of increase of CO mass above 8 km is not uniform, but varies significantly in time. There are peaks at early times, followed by a decline and minimum as the system transitions to a supercell, followed by a steady increase as the storm evolves into a supercell. At the final time, the supercell was pumping over half as much CO into the upper atmosphere (i.e., above 8 km) as were three to four cells at earlier times.

Trajectory analyses show that convective updrafts in the simulation are ingesting air from a layer spanning approximately 0.5 - 2 km above the ground (2 - 3.5 km msl), and we find that boundary layer air closest to the ground (below $\sim$ 0.5 km above the ground) is not being drawn into the convective updrafts. Most parcels reside in the updrafts for a time varying from just under 10 min to more than 20 min, with most common residence time of around 10 min. Lastly, wind profile analyses reveal that there is significant curvature in the hodograph over the lowest 2 km for this event, with southeast winds at the surface veering to north-northwesterly flow above 3.5 km msl (2 km above the surface). Thus the simulation suggests that the inflow to the July 10 STERAO convective system air was predominately from the west and southwest. This characteristic of the inflow, that is, that the storm-processed air does not originate below 500 m, is difficult to document with the observations, but may be common in summertime high plains convection. Similar modeling investigations of other STERAO events are under way and may confirm this finding.

Acknowledgments. W.C.S. is partially supported under the NOAA Climate and Global Change Program award NA76GP00400. The UND Citation effort was supported under National Science Foundation (NSF) grant ATM-9634125. The CSU-CHILL national radar facility is supported by the National Science Foundation and Colorado State University. The National Center for Atmospheric Research is sponsored by the National Science Foundation.

References

Dye, J. E., et al., An overview of the Stratospheric-Tropospheric Experiment: Radiation, Aerosols, and Ozone (STERAO) – Deep Convection Experiment with results for the July 10,1996 storm, *J. Geophys. Res.*, *105*, 10,023-10,045, 2000.

Hauf, T., P. Schulte, R. Alheit, , and H. Schlager, Rapid vertical transport by an isolated midlatitude thunderstorm, *J. Geophys. Res.*, *100*, 22,957–22,970, 1995.

Jorgenson, D. P., T. Matejka, and J. D. DuGranrut, Multi-beam techniques for deriving wind fields from airborne doppler radars, *Meteorol. Atmos. Phys.*, *59*, 83–104, 1996.

Knupp, K. R., Downdrafts within high plains cumulonimbi. part i: General kinematic structure, *J. Atmos. Sci.*, *44*, 987–1008, 1987.

Logan, A. J., An analysis of ozonesonde data for the troposphere: Recommendations for testing 3-d models and development of a gridded climatology for tropospheric ozone, *J. Geophys. Res.*, *104*, 16,115–16,149, 1999.

Pickering, K. E., J. R. Scala, A. M. Thompson, W.-K. Tao, and J. Simpson, A regional estimate of convective transport of co from biomass burning, *Geophys. Res. Lett.*, *19*, 289–292, 1992a.

Pickering, K. E., A. M. Thompson, J. R. Scala, W.-K. Tao, R. R. Dickerson, and J. Simpson, Free tropospheric ozone production following entrainment of urban plumes into deep convection, *J. Geophys. Res.*, *97*, 17,985–18,000, 1992b.

Scala, J. R., et al., Cloud draft structure and trace gas transport, *J. Geophys. Res.*, *95*, 17,015–17,030, 1990.

Skamarock, W. C., M. L. Weisman, and J. B. Klemp, Three-dimensional evolution of simulated long-lived squall lines, *J. Atmos. Sci.*, *51*, 2563–2584, 1994.

Stenchikov, G. R., R. Dickerson, K. Pickering, W. E. Jr., B. Doddridge, S. Kondragunta, and O. Poulida, Stratosphere-troposphere exchange in a midlatitude mesoscale convective complex. 2. Numerical simulations, *J. Geophys. Res.*, *101*, 6837–6851, 1996.

Tao, W.-K., and J. Simpson, Goddard cumulus ensemble model. Part I: Model description, *TAO*, *4*, 35–72, 1993.

Thompson, A. M., K. E. Pickering, R. R. Dickerson, W. G. E. Jr., D. J. Jacob, J. R. Scala, W.-K. Tao, D. P. McNamara, and J. Simpson, Convective transport over the central united states and its role in regional co and ozone budgets, *J. Geophys. Res.*, *99*, 18,703–18,711, 1994.

Wang, C., and J. S. Chang, A three dimensional numerical model of cloud dynamics, microphysics, and chemistry. 3. Redistribution of pollutants, *J. Geophys. Res.*, *98*, 16,787–16,798, 1993.

Wang, C., and P. J. Crutzen, Impact of a simulated severe local storm on the redistribution of sulfer dioxide, *J. Geophys. Res.*, *100*, 11,357–11,367, 1995.

Wang, C., P. J. Crutzen, and V. Ramanathan, The role of a deep convective storm over the tropical pacific ocean in the redistribution of atmospheric chemical species, *J. Geophys. Res.*, *100*, 11,509–11,516, 1995.

Weisman, M. L., and J. B. Klemp, The dependence of numerically simulated storms on vertical wind shear and buoyancy, *Mon. Weather. Rev.*, *110*, 504–520, 1982.

Wicker, L. J., and W. C. Skamarock, A time splitting scheme for the elastic equations incorporating second-order runge-kutta time differencing, *Mon. Weather. Rev.*, *126*, 1992–1999, 1998.

Wicker, L. J., and R. B. Wilhelmson, Simulation and analysis of tornado development and decay within a three-dimensional supercell thunderstorm, *J. Atmos. Sci.*, *52*, 2675–2703, 1995.

D. Bartels, and T. Matejka, NOAA Severe Storms Laboratory, 325 Broadway, Boulder, CO 80303.

M. Barth, J. E. Dye, J. G. Powers, W. C. Skamarock, and J. Stith, National Center for Atmospheric Research, P. O. Box 3000, Boulder, CO 80307-3000. (skamaroc@ucar.edu)

K. Baumann, Department of Earth and Atmospheric Science, Georgia Institute of Technology, 221 Bobby Dodd Way, Atlanta, GA 30332.

G. Hubler, and D. D. Parrish, NOAA Aeronomy Laboratory, 325 Broadway, Boulder, CO 80303.

(Received February 5, 1999; revised January 27, 2000; accepted January 29, 2000.)